



City Research Online

City St George's, University of London

Citation: Kechagias-Stamatis, O., Aouf, N. & Richardson, M. A. (2019). High-speed multi-dimensional relative navigation for uncooperative space objects. *Acta Astronautica*, 160, pp. 388-400. doi: 10.1016/j.actaastro.2019.04.050

This is the accepted version of the paper.

This version of the publication may differ from the final published version. To cite this item please consult the publisher's version.

Permanent repository link: <https://openaccess.city.ac.uk/id/eprint/23173/>

Link to published version: <https://doi.org/10.1016/j.actaastro.2019.04.050>

Copyright and Reuse: Copyright and Moral Rights remain with the author(s) and/or copyright holders. Copies of full items can be used for personal research or study, educational, or not-for-profit purposes without prior permission or charge, unless otherwise indicated, provided that the authors, title and full bibliographic details are credited, a hyperlink and/or URL is given for the original metadata page and the content is not changed in any way. For full details of reuse please refer to [City Research Online policy](#).

High-Speed Multi-dimensional Relative Navigation for Uncooperative Space Objects

O. Kechagias-Stamatis ^{a,*}, N. Aouf ^b and M. A. Richardson ^a

^a Centre of Electronic Warfare, Cranfield University Defence and Security, Shrivenham, SN6 8LA, UK

^b Department of Electrical and Electronic Engineering, City University of London, EC1V 0HB, UK

Abstract

This work proposes a high-speed Light Detection and Ranging (LIDAR) based navigation architecture that is appropriate for uncooperative relative space navigation applications. In contrast to current solutions that exploit 3D LIDAR data, our architecture transforms the odometry problem from the 3D space into multiple 2.5D ones and completes the odometry problem by utilizing a recursive filtering scheme. Trials evaluate several current state-of-the-art 2D keypoint detection and local feature description methods as well as recursive filtering techniques on a number of simulated but credible scenarios that involve a satellite model developed by Thales Alenia Space (France). **Most appealing performance is attained by the 2D keypoint detector Good Features to Track (GFFT) combined with the feature descriptor KAZE, that are further combined with either the H_∞ or the Kalman recursive filter. Experimental results demonstrate that compared to current algorithms, the GFFT/ KAZE combination is highly appealing affording one order of magnitude more accurate odometry and a very low processing burden, which depending on the competitor method, may exceed one order of magnitude faster computation.**

Keywords: Multi-dimensional processing, Relative navigation, Spaceborne LIDAR, Uncooperative target

1

2 1. Introduction

3 Ego-motion estimation, i.e. odometry, for space applications is an active research domain due to the increasing
4 number of spacecrafts deployed. Specifically, great research interest considers relative space navigation of a *Source*
5 spacecraft platform in relation to a non-cooperative *Target* platform, i.e. with unknown attitude (pose). This is
6 because relative space navigation will enable a *Source* spacecraft with the capability to perform autonomous close-

* Corresponding author

E-mail address: [o.kechagiasstamatis @Cranfield .ac.uk](mailto:o.kechagiasstamatis@Cranfield.ac.uk)

7 proximity manoeuvres and achieve uncooperative rendezvous with a non-cooperative *Target* platform, contributing
8 towards autonomous active space debris removal, satellite inspection and docking. In any of these scenarios, the
9 *Target* is likely to be non-cooperative and therefore unable to exchange with the *Source* its **pose neither actively nor**
10 **passively**, i.e. via known markers placed on the *Target*. Therefore, the *Source* spacecraft must estimate its relative
11 position and attitude with respect to the *Target* platform by utilizing only its onboard sensors. Current solutions
12 involve 2D visual data in a monocular [1,2] or a stereo camera configuration [3–6], 2D Infrared (IR) thermal data
13 [7], and 3D Light Detection and Ranging (LIDAR) data [8,9,18,10–17]. A thorough review of spacecraft pose
14 determination techniques for close-proximity operations is presented in [19].

15 Despite each modality, i.e. visual, IR and LIDAR, having its own strengths and weaknesses, LIDAR is preferred
16 either in a scanning or in a flash operating mode due to its proven robustness in the space environment [20]. Indeed,
17 visual data can be an effective solution [21] but the use of IR data have several advantages over the visual data
18 because they can operate during day and night under several harsh illumination conditions like eclipse and solar
19 glare. Despite these advantages, the accuracy of IR thermal odometry relies on the *Target's* temperature that is
20 affected by internal parameters, e.g. heat dissemination of the platform's components, and external parameters, e.g.
21 reflection of sun's radiation. This temperature fluctuation can affect the robustness of the IR based local feature
22 detection and matching process, which are the core procedures of the IR thermal odometry presented in [7]. On the
23 contrary, 3D LIDAR based odometry **outperforms** its 2D counterparts (visual and IR) as it operates during day, night
24 and under poor visibility conditions, is independent of the *Target's* thermal properties, is capable of revealing the
25 underlying structure of an object and can provide both 3D position and intensity data. [19,22].

26 Despite the advantages of LIDAR, the associated hardware requirements for power, physical space and the
27 corresponding computational cost of the algorithms used are higher compared to 2D based architectures exploiting
28 visual or IR sensors. This is because LIDAR sensors are complex active devices involving 3D data manipulation,
29 while visual and IR cameras are passive and less complex devices that in principle output 2D data. However,
30 spurred by the advantages of LIDAR odometry, LIDAR sensors have already been placed on space platforms [23]
31 trading off the amplified requirements of this type of sensors with their advantages over visual and IR cameras. An
32 open case is the processing recourses onboard space platforms that are typically based on space-graded field
33 programmable gate arrays (FPGA). However, recent work [24] demonstrated that FPGA boards are capable of
34 performing 2D computer vision based navigation. Hence, there is the potential for FPGA boards to perform complex

35 space navigation utilizing 3D LIDAR data. For further details on spaceborne sensors for spacecraft pose estimation
36 the reader is referred to [19].

37 Spurred by the advantages of 3D LIDAR odometry for space applications, current literature suggests quite a few
38 techniques that are summarized in Table 1. Specifically, [13] presents the capabilities of the *Argon* relative
39 navigation system that uses a stereo optical camera and a flash LIDAR configuration. *Argon* application relies on
40 edge detection and a custom Iterative Closest Point (ICP) scheme for 6-degrees of freedom pose estimation. Other
41 solutions involve template matching for pose initialization and then exploit the typical ICP [25] for frame-to-frame
42 pose estimation [9,16,17,26,27]. Variants of that methodology substitute the template matching scheme for pose
43 initialization either with Principle Component Analysis (PCA) [9,28] or with global 3D feature matching using the
44 Oriented Unique Repeatable Clustered Viewpoint Feature Histogram (OUR-CVFH) [14,29]. Other solutions
45 available in the literature fuse pose estimation based on OUR-CVFH or on Spin Images [30] (a 3D local feature
46 descriptor) and ICP, with gyroscopic data and then perform *Target* platform tracking using a Multiplicative
47 Extended Kalman Filter (MEKF) [10,28,31]. Volpe *et al.* [11] suggest utilizing 2D features from the visual domain
48 combined with LIDAR based distance estimation and Unscented Kalman Filtering (UKF) for performance
49 improvement. Alternatives to pure ICP registration for pose estimation have also been proposed by substituting ICP
50 with a UKF filter, an iterative least-squares (LS) scheme, or with an Extended Kalman Filter (EKF) [32], [33]. An
51 additional alternative is suggested in [18] that combines 3D local feature matching based on the Histogram of
52 Distances – Short (HoD-S) descriptor [34] and the H_∞ filter.

53 Driven by the advantages of 3D LIDAR odometry, the availability of affordable LIDAR technologies and
54 considering the need for space odometry with increased accuracy and less computational burden, we suggest a novel
55 LIDAR based architecture that transforms the odometry problem from the 3D space into multiple 2D ones that
56 involve 2.5D imagery (range maps) and completes the odometry problem by utilizing a recursive filtering technique.
57 Specifically, in the context of uncooperative space odometry the contributions of this work are:

58 a. A high-speed space odometry architecture that has a processing burden in the order of milliseconds and
59 provides one order of magnitude more accurate relative odometry compared to current solutions.

60 b. A multi-dimensional solution that combines the advantages of the 2D and 3D data space. Indeed, our
61 architecture reaches high odometry accuracy as it exploits 3D data and a very low processing time due to

transforming the odometry problem from the 3D space into multiple 2D ones that involve 2.5D imagery to minimize information loss.

c. It evaluates state-of-the-art local keypoint detection, feature description and recursive filtering methods and analyses their performance.

The remainder of the article is organized as follows: Section 2 introduces the proposed LIDAR based space odometry architecture and extensively presents the evaluation of 2D keypoint detectors, feature descriptors and recursive filtering methodologies. Section 3 evaluates the suggested architecture against current LIDAR based odometry methods on several simulated but highly realistic scenarios and our conclusions are presented in Section 4.

Table 1.
Current 3D space odometry architectures

N ^o	Reference	Year	Target	Hardware	Relative navigation method
1	Galante <i>et al.</i> [13]	2012	Real	Stereo optical camera and LIDAR	2D edge tracking and custom ICP for pose estimation
2	Sell <i>et al.</i> [14]	2014	Real	LIDAR	OUR-CVFH for pose initialization and ICP for point cloud registration and pose estimation
3	Opromolla <i>et al.</i> [16]	2014	Simulated	LIDAR	Optimized template matching for pose initialization and ICP for point cloud registration and pose estimation
4	Opromolla <i>et al.</i> [17,26]	2015	Simulated	LIDAR	Optimized template matching for pose initialization and ICP for point cloud registration and pose estimation
5	Rhodes <i>et al.</i> [28]	2016	Simulated	Gyroscope, star tracker, LIDAR	OUR-CVFH or Spin Images combined with ICP for pose estimation that is fused with sensor inputs via a MEKF module
6	Liu, Zhao and Bo [27]	2016	Simulated and real	LIDAR	Template based pose initialization and ICP object tracking
7	Woods and Christian [10]	2016	Simulated	Gyroscope, GPS, star tracker, LIDAR	OUR-CVFH for pose initialization and ICP for point cloud registration and pose estimation that is fused with sensor inputs via a MEKF module
8	Opromolla <i>et al.</i> [9]	2017	Real	LIDAR	Optimized template matching or PCA for pose initialization and ICP for point cloud registration and pose estimation
9	Volpe <i>et al.</i> [11]	2017	Simulated	Optical camera and LIDAR	2D feature based visual odometry with LIDAR based distance measurement combined with UKF
10	Rhodes, Christian and Evans [31]	2017	Simulated	LIDAR	OUR-CVFH or OUR-CVFH combined with MEKF for trajectory smoothing
11	Dietrich and McMahan [33]	2017	Simulated	LIDAR	point cloud registration using UKF
12	Dietrich and McMahan [32]	2018	Simulated	LIDAR	point cloud registration using UKF, LS and EKF
13	Kechagias-Stamatis and Aouf [18]	2019	Real	LIDAR	HoD-S local features with adaptive H ∞ recursive filtering

2. Proposed Architecture

2.1. LIDAR based Odometry

The suggested LIDAR based relative navigation architecture involves a *Source* platform that has a 3D LIDAR sensor and an uncooperative *Target* platform with an unknown structure. The aim of the proposed technique is to estimate the relative position between the *Source* platform and the *Target* platform, with equal priority given to position accuracy and computational requirements.

78 Given two consecutive point clouds $\mathbf{P}_k = \{p_k^1, \dots, p_k^a\}$ and $\mathbf{P}_{k+1} = \{p_{k+1}^1, \dots, p_{k+1}^b\}$ of the *Target* platform that are
 79 captured from the *Source*'s LIDAR sensor, with each vertex being in the form $p = (x, y, z)$, the odometry process
 80 aims at calculating a rigid body transformation,

$$81 \quad R^* = \begin{bmatrix} R & T \\ 0 & 1 \end{bmatrix} \quad (1)$$

82 with R as the rotation and T the translation component that remap point cloud \mathbf{P}_k to \mathbf{P}_{k+1} :

$$83 \quad p_{k+1} = R p_k + T \quad (2)$$

$$84 \quad \begin{bmatrix} x_{k+1} \\ y_{k+1} \\ z_{k+1} \end{bmatrix} = \begin{bmatrix} r_{11} & r_{12} & r_{13} \\ r_{21} & r_{22} & r_{23} \\ r_{31} & r_{32} & r_{33} \end{bmatrix} \begin{bmatrix} x_k \\ y_k \\ z_k \end{bmatrix} + \begin{bmatrix} T_x \\ T_y \\ T_z \end{bmatrix} \quad (3)$$

85 Then at instance u , the position of the *Source* platform relative to the unknown and uncooperative *Target* is given
 86 by:

$$87 \quad R_u^* = \prod_{\mu=1}^u R_\mu^* \quad (4)$$

88 Current literature addresses LIDAR odometry for space applications mainly by calculating R^* via a two-staged
 89 process, i.e. coarse *Target* pose initialization using template matching or 3D feature matching (global or local
 90 features), and then perform *Target* pose estimation via an ICP process. However, as presented in Section 3, **these**
 91 **solutions still exhibit certain challenges including** low odometry accuracy and high processing burden.

92 2.2. Multi-Projection LIDAR Odometry

93 Driven by the need of achieving a high **performance** and efficient uncooperative relative navigation architecture,
 94 we suggest an appealing multi-discipline architecture, which accurately estimates the transformation R^* with a very
 95 low computational burden. An analysis of the developed approach is presented in the following paragraphs of this
 96 section.

97 2.2.1 Multi-2.5D local keypoint detection, description, and matching

98 **Although** 3D data have several advantages over their 2D counterpart (see Section 1), the computational burden
 99 to manipulate 3D data is substantially higher compared to exploiting 2D data [35]. Therefore, we take advantage of
 100 both data modalities by remapping \mathbf{P}_k and \mathbf{P}_{k+1} into several 2.5D images, i.e. 2D range maps/ images. Specifically,
 101 for \mathbf{P}_k and accordingly for \mathbf{P}_{k+1} , we transfer the XYZ_{LIDAR} reference frame that is centred at the LIDAR sensor
 102 onboard the *Source* platform to \mathbf{P}_k and create the XYZ_{Target} reference frame. Then, we quantize the floating-point
 103 vertex coordinates $\mathbf{P}_k = \{p_k^1, \dots, p_k^a\}$ into $\mathbf{P}_{Q-k} = \{p_{Q-k}^1, \dots, p_{Q-k}^a\}$ with,

$$104 \quad p_{Q-k}(x_Q, y_Q, z_Q) = \lfloor q_f \cdot p_k(x, y, z) \rfloor \quad (5)$$

105 where q_f is a quantization factor and $\lfloor \cdot \rfloor$ the bottom-round process. Next, we multi-project \mathbf{P}_{Q-k} to every plane of
 106 the XYZ_{Target} reference frame by utilizing an orthographic projection process P_{ortho} . Depending on the projection
 107 plane, we substitute with zero the appropriate binary remapping coefficients $c_1, c_2, c_3 \in \{0, 1\}$ of P_{ortho} , i.e. for
 108 $c_1 = c_2 = 1$ and $c_3 = 0$, the XY 2.5D image coordinates \tilde{p}_{Q-k} are created:

$$109 \quad \tilde{p}_{Q-k} = \begin{bmatrix} \tilde{x}_q \\ \tilde{y}_q \\ \tilde{z}_q \\ 1 \end{bmatrix} = P_{ortho} \cdot p_{Q-k} = \begin{bmatrix} c_1 & 0 & 0 & 0 \\ 0 & c_2 & 0 & 0 \\ 0 & 0 & c_3 & 0 \\ 0 & 0 & 0 & 1 \end{bmatrix} \cdot \begin{bmatrix} x_{Q-k} \\ y_{Q-k} \\ z_{Q-k} \\ 1 \end{bmatrix} \quad (6)$$

110 The three orthographic projections $\tilde{p}_{Q-k}^{XY}, \tilde{p}_{Q-k}^{XZ}, \tilde{p}_{Q-k}^{YZ}$ are 2.5D images, which are simplified versions of \mathbf{P}_{Q-k} .
 111 The depth value of each \tilde{p}_{Q-k} is unique and represents the distance between the target and the LIDAR sensor. An
 112 example of the multi-2.5D process is presented in Fig. 1.

113 Next on each 2.5D image we apply current state-of-the-art 2D keypoint detection methods to analyse the
 114 structure around each pixel and classify as keypoints the ones that fulfil some specific criteria that depend on the
 115 detector. Ideally, keypoints are prominent among their surroundings, have unique features, and can be redetected
 116 even if the object they belong to is distorted or corrupted. Despite literature offering quite a few 2D keypoint
 117 detection methods, for better readability in this work we evaluate one representative of the two main keypoint
 118 detection categories, namely *blob* and *corner* detectors. Since in this work, keypoint detection performance and
 119 processing efficiency are of equal importance, for the former category we select the Fast Hessian (FH) [36] and the

120 for the latter the Good Features To Track (GFTT) [37]. For completeness we present the operating principle of each
 121 keypoint detector evaluated.
 122

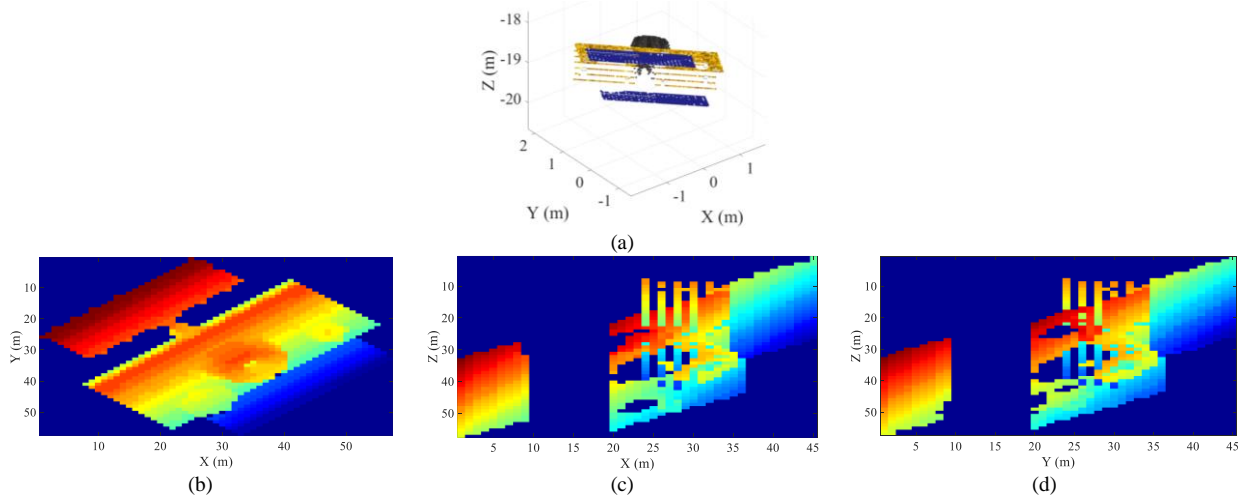


Fig. 1. 3D to multi 2.5D projection, a) 3D point cloud data in the XYZ_{Target} reference frame, (b)-(d) multi-2.5D imagery (red corresponds to close and blue to far $Source - Target$ platform distance)

123
 124 **Fast Hessian (FH)** [36] neglects the processing burden of convolving the input image with second-order
 125 derivatives by approximating the Gaussian kernels with their discretized version (i.e. box filters) that are computed
 126 with a constant time cost by utilizing the integral image concept [39]. Candidate features are obtained after a $3 \times 3 \times$
 127 3 neighbourhood non-maximum suppression process and the ones with a response Rp exceeding a pre-defined
 128 threshold are preserved while the rest are discarded:

$$129 \quad Rp(x, y, \sigma) = D_{xx}(\sigma)D_{yy}(\sigma) - (0.9D_{xy}(\sigma))^2 \quad (7)$$

130 where $D_{xx}(\sigma)$, $D_{yy}(\sigma)$ and $D_{xy}(\sigma)$ are the outputs after convolving the corresponding box filters of standard
 131 deviation σ with each 2.5D image $I = \tilde{p}_{Q-k}^{XY}, \tilde{p}_{Q-k}^{XZ}, \tilde{p}_{Q-k}^{YZ}$.

132 **The Good Features To Track (GFTT)** keypoint detector [37] relies on an autocorrelation function that captures the
 133 intensity variations of an image I in a neighbourhood window Q centred at pixel $p(x,y)$:

$$134 \quad E(x, y) = \sum_Q w(u, v) [I(u+x, v+y) - I(u, v)]^2 \quad (8)$$

135 where (x, y) are the pixel coordinates in I , and $w(u, v)$ is the window patch at position (u, v) . Using Taylor's
 136 approximation, Eq. (8) becomes:

137
$$E(x, y) = \begin{bmatrix} x & y \end{bmatrix} M \begin{bmatrix} x \\ y \end{bmatrix} \quad (9)$$

138
$$M = \begin{bmatrix} \sum_Q I_u^2 & \sum_Q I_u I_v \\ \sum_Q I_u I_v & \sum_Q I_v^2 \end{bmatrix} \quad (10)$$

139 where I_u, I_v represent the spatial gradients of the image.

140 The shape of Q is classified based on the eigenvalues λ_1 and λ_2 of M . Specifically, if both values are small, E also
 141 has a small value and Q has an approximately constant intensity. If both are large, E has a sharp peak indicating that
 142 Q includes a corner, if $\lambda_1 > \lambda_2$ then Q includes an edge and if $\min(\lambda_1, \lambda_2) > \lambda$, then Q encloses a corner, where λ is a
 143 predefined threshold. To measure the corner or edge quality, metric R_G is used:

144
$$R_G(x, y) = \det(M) - k \cdot \text{tr}(M) = \lambda_1 \lambda_2 - k(\lambda_1 + \lambda_2) \quad (11)$$

145 where $k \in [0.04, \dots, 0.15]$.

146 After detecting keypoints on the 2.5D images I , each keypoint is encoded using a local feature description
 147 technique, which aims at encoding the properties of a local patch centred on each keypoint. Ideally, feature
 148 descriptors describe each keypoint in a unique manner and are robust to orientation variations and affine
 149 transformations. Given that odometry accuracy and processing efficiency are of equal importance, we evaluate the
 150 SURF [36], KAZE [41], Fast Retina Keypoint (FREAK) [42] and the Binary Robust Invariant Scalable Keypoints
 151 (BRISK) [43] feature descriptors. It should be noted that we carefully select the feature descriptor candidates such
 152 that both floating point (SURF and KAZE) and binary class (FREAK and BRISK) descriptors **are included in order**
 153 **to evaluate not** only each descriptor individually, but also the overall performance of each class. It is worth noting
 154 that despite the Scale Invariant Feature Transform (SIFT) [38] method being unarguably one of the most robust
 155 feature descriptors, its computational burden is higher compared to the floating point descriptors SURF and KAZE
 156 [41] and is therefore discarded. For completeness we present the operating principle of each descriptor evaluated.

157 SURF [36] initially performs an orientation assignment by computing Gaussian-weighted Haar wavelet responses
 158 over a circular region with a radius six times the scale where the keypoint is detected. Once an orientation is
 159 assigned, a square region ($20 \times \text{scale}$) is centred on the keypoint, oriented accordingly and is then further divided
 160 into 4×4 sub-regions. For each sub-region vertical and horizontal Haar-wavelet responses weighted with a Gaussian
 161 kernel are computed. This process is performed at fixed sample points and is summed up in each sub-region. Finally,

162 the polarity of intensity changes is also calculated by summing the absolute values of the horizontal and vertical
 163 responses. SURF features of opposing polarity are not matched. The keypoint description part of KAZE [41] is
 164 similar to SURF but is properly adapted to facilitate a non-linear scale-space framework, rather than a linear that is
 165 used in SURF.

166 The BRISK method [43] encodes keypoints using a handcrafted sampling pattern comprising of concentric
 167 circular patches centred at a keypoint. Aliasing effects during sampling are avoided by applying local Gaussian
 168 smoothing on the patch to be described, with a standard deviation proportional to the distance between the circle
 169 centre and the keypoint. There are two types of sampling pairs (short and long pairs) that depend on the distance
 170 between them. The long pairs have a distance greater than threshold d_{min} and are used to compute the local gradient
 171 (of the patch) that defines the orientation of the feature. The short pairs with a distance less than threshold d_{max} are
 172 then rotated accordingly to achieve rotation invariance and are used to compute the binary BRISK descriptor via
 173 intensity tests.

174 FREAK [42] is a biologically-inspired binary descriptor that applies a series of intensity tests on a patch that is
 175 centred at the keypoint. FREAK and BRISK share the same sampling pattern and use the same mechanism to
 176 estimate the keypoint orientation. However, FREAK is influenced by the human retinal system and uses a circular
 177 sampling grid with sampling points that are denser near the centre and become exponentially less dense further away
 178 from the centre. The advantage of this concept is that the test pairs naturally form a coarse-to-fine approach. Feature
 179 matching is accelerated by comparing the coarse part of the descriptor and if these exceed a threshold then the fine
 180 part is tested.

181 Once we describe all keypoints, we then employ a feature matching stage that cross-matches all features
 182 originating from every 2.5D image projection of both \mathbf{P}_k and \mathbf{P}_{k+1} . This strategy involves cross-matching all nine
 183 2.5D image projection combinations compensating a high-speed relative motion between the *Source* and the *Target*
 184 platform where a keypoint during the multi-projection process might shift from one 2.5D image to another. Let
 185 $\mathbf{F}_k = \{f_k^1, \dots, f_k^{N_i}\}$ and $\mathbf{F}_{k+1} = \{f_{k+1}^1, \dots, f_{k+1}^{N_j}\}$ be two sets of features belonging to the 2.5D images of point clouds \mathbf{P}_k
 186 and \mathbf{P}_{k+1} , respectively. We match feature f_k^i from \mathbf{F}_k with its nearest feature f_{k+1}^j from \mathbf{F}_{k+1} based on an L₂-norm
 187 metric:

$$188 \quad f_k^i \triangleq f_{k+1}^j \longleftarrow \arg \min_{n=1,2,\dots,N_j} \left(\|f_k^i - f_{k+1}^n\|_2 \right) < \tau \quad (12)$$

189 where u, j are the feature indexes and the threshold τ is set to 1 to reduce the dependency between the threshold
190 value and the metric used [44]. We speedup the process of Eq. (12) by employing the Fast Library for Approximate
191 Nearest Neighbors (FLANN) [45]. **FLANN is a library that is used for fast approximate nearest neighbour searches**
192 **in high dimensional spaces. It either uses a hierarchical k-means trees search with a priority search order or a**
193 **multiple randomized kd-trees scheme. The selection of the search scheme and the optimum parameters are**
194 **automatically chosen from the FLANN library and depend on the data applied to FLANN.** Feature matching is then
195 performed by extending the geometric consistency checks of [46] in the 2.5D domain. Specifically, the
196 correspondences obtained from FLANN (Eq. (12)) are clustered into hypotheses, using their true physical geometric
197 (pixel distance) consistency. Geometric consistency aims at reducing mismatches by grouping correspondences into
198 clusters that are geometrically consistent. For the latter, from the FLANN matching stage (Eq. (12)) a list of
199 descriptor correspondences is created $H_u = \{P_{Q-k}^u, P_{Q-k+1}^u\}$, where P_{Q-k}^u and P_{Q-k+1}^u are the *Target* correspondences
200 in pixel coordinates at instance k and $k+1$:

$$201 \quad H_u = \{P_{Q-k}^u, P_{Q-k+1}^u\} \longleftarrow f_k^i \hat{=} f_{k+1}^j \quad (13)$$

202 Given a seed correspondence from H_u , the first cluster is initialized and all correspondences $H_v = \{P_{Q-k}^v, P_{Q-k+1}^v\}$,
203 $v < u$ not yet grouped that are geometrically consistent with the cluster are added to it. The consistency check for a
204 pair of correspondences H_u, H_v is valid if the following distance relation holds:

$$205 \quad \left| \|P_{Q-k}^u - P_{Q-k}^m\|_2 - \|P_{Q-k+1}^u - P_{Q-k+1}^m\|_2 \right| < \varepsilon \quad (14)$$

206 ε being the threshold tolerance for their consensus set. The matched feature pairs $\{f_k^i, f_{k+1}^j\}$ belonging to the cluster
207 with the largest cardinality are considered as feature matches, while their associated vertices $\Omega_Q = \{P_{Q-k}^i, P_{Q-k+1}^j\}$
208 are considered as point correspondences. Finally, we back-project Ω_Q to the initial 3D space and establish a set of
209 3D correspondences $\Omega = \{P_k^i, P_{k+1}^j\}$. Due to the quantization process of Eq. (5), we create Ω by correlating each
210 back-projected vertex pair of Ω_Q to its nearest neighbour vertex in P_k and P_{k+1} respectively.

211 2.2.2 Recursive filtering

212 We solve Eq. (2) utilizing a recursive filtering scheme where the state variable
 213 $x_k = [r_{11} \ r_{12} \ r_{13} \ r_{21} \ r_{22} \ r_{23} \ r_{31} \ r_{32} \ r_{33} \ t_x \ t_y \ t_z]^T$ encompasses the rigid transformation between \mathbf{P}_k and \mathbf{P}_{k+1} by exploiting
 214 the correspondences Ω . It should be noted that we intentionally do not apply the recursive filtering scheme in the
 215 2D space by exploiting Ω_Q as this would increase the overall processing time due to the feature cross-matching
 216 approach. In this paper we evaluate the H_∞ and the Kalman recursive filters.

217 H_∞ filter [47] is a recursive optimal state estimator that is adapted to our formulated registration model with x_k
 218 the state variable vector and $\psi_k = [x_k, y_k, z_k]^T$ the measurement vector that contains the 3D coordinates of the point
 219 correspondences p_{k+1}^j belonging to \mathbf{P}_{k+1} , which are included in Ω . The registration model is given then by:

$$220 \quad x_k = \Phi x_{k-1} + w_{k-1} \quad (15)$$

$$221 \quad \psi_{k+1} = H_k x_k + v_k \quad (16)$$

222 where Φ is the state transition matrix and H the measurement model matrix. We set $\Phi = R_0^* = [I \ | \ T_0]$ with I the
 223 identity matrix and $T_0 = [0 \ 0 \ 0]^T$, w and v are the model and the measurement noise factors respectively with
 224 covariance matrices $W \sim N(0, \sigma_w^2 J_{12})$ and $V \sim N(0, M \sigma_v^2 J_3)$ where σ_w and σ_v are small positive values and J is
 225 the unity matrix. H_k contains the actual measured 3D coordinates of p_k^i belonging to \mathbf{P}_k that are included in Ω :

$$226 \quad H_k = \begin{bmatrix} x_{k+1} & y_{k+1} & z_{k+1} & 0 & 0 & 0 & 0 & 0 & 0 & 1 & 0 & 0 \\ 0 & 0 & 0 & x_{k+1} & y_{k+1} & z_{k+1} & 0 & 0 & 0 & 0 & 1 & 0 \\ 0 & 0 & 0 & 0 & 0 & 0 & x_{k+1} & y_{k+1} & z_{k+1} & 0 & 0 & 1 \end{bmatrix} \quad (17)$$

227 The problem that the H_∞ filter is trying to solve is the $\min_x \max_{w,v} G$ where G is defined as:

$$228 \quad G = \frac{\text{average}(\|x_k - x_k\|)_Q}{\text{average}(\|w_k\|)_W + \text{average}(\|v_k\|)_V} \quad (18)$$

229 subject to $G < 1/\gamma$, with Q being a weighting matrix and γ a small constant representing the required accuracy of
 230 the filter. The H_∞ filter equations solving Eq. (18) are:

231
$$L_k = \left(I - gQP_{k-1} + H_k^T V^{-1} H_k P_{k-1} \right)^{-1} \quad (19)$$

232
$$K_k = \Phi P_{k-1} L_k H_k^T V^{-1} \quad (20)$$

233
$$P_k = \Phi P_{k-1} L_k \Phi^T + W \quad (21)$$

234
$$x_{k+1} = \Phi x_k + K_k \left(\psi_k - H_k x_k \right) \quad (22)$$

235 where $Q = Idt$ with $dt = 10^{-5}$ and $g = 0.1$ being regulating parameters. The number of iterations of the H_∞ filter is
 236 the cardinality of Ω and ultimately the final x is transformed into R^* after all iterations, which is input to Eq. (4) in
 237 order to estimate the LIDAR based odometry. The parameters of the H_∞ filter as well as rest of the filters evaluated
 238 in this work are calibrated based on scenario 1.

239 We also evaluate the performance of the Kalman filter [48], which using the same notation as for the H_∞
 240 filter, is given by:

241
$$x_k = \Phi x_{k-1} + Bq_k + w_{k-1} \quad (23)$$

242
$$\psi_k = H_k x_k + v_k \quad (24)$$

243 with B as the control input model matrix and q the control vector of the system. The *Kalman* filter equations are:

244
$$K_k = AP_k H_k^T \left(H_k P_k H_k^T + VM \right)^{-1} \quad (25)$$

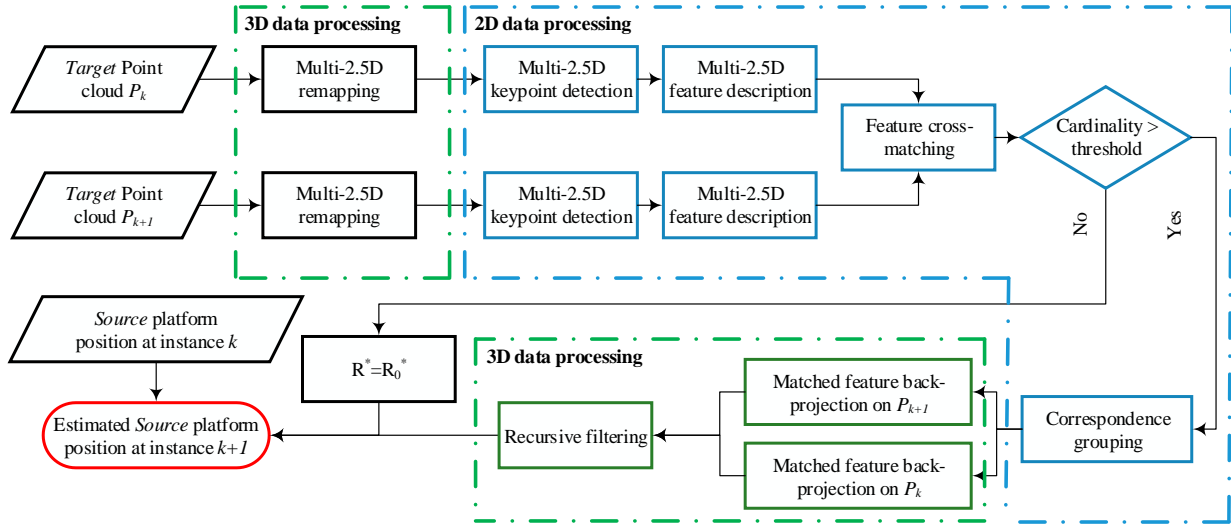
245
$$x_{k+1} = \left(\Phi x_k + Bu_k \right) + K_k \left(\psi_k - H_k x_k \right) \quad (26)$$

246
$$P_k = \Phi P_{k-1} \Phi^T + W - \Phi P_{k-1} H_k^T V^{-1} H_k P_{k-1} \Phi^T \quad (27)$$

247 where K is the Kalman gain and P the estimation error covariance, with $\sigma_v = 1$ and $\sigma_w = 5 \cdot 10^{-3}$ that are
 248 experimentally defined on scenario 1 to gain optimum odometry performance.

249 It should be noted that depending on the *Target's* pose at instance k and $k+1$, the multi-projection and feature
 250 cross-matching process may provide correspondences with a cardinality that is not adequate for the recursive

251 filtering process to iterate properly and estimate R^* accurately. Thus, in case the correspondence cardinality is below
 252 a pre-defined threshold, we input the initialization value $R = R_0^*$ to the Eq. (1). The suggested architecture is
 253 presented in Fig. 2.
 254



255
 256
 257
 258 **Fig. 2.** Suggested recursive LIDAR odometry

3. Experiments

3.1 Experimental Setup

259 For our trials we use simulated trajectories of a space platform that is a customized version inspired from the
 260 Globalstar-2 and Iridium constellations, based on the Elite platform developed by Thales Alenia Space (France). In
 261 our trials we consider three scenarios, namely a straight-line approach (SLA), an ellipse of inspection (EOI) and a
 262 static station keeping (SSK). In order to increase the realistic nature of the trials, simulation considers the Earth's
 263 mass, the Sun's sunlight power with respect to each spectral band and the typical physical size of the *Source* and the
 264 *Target* platforms. An example of the *Target* platform along with the ground truth trajectory of the SLA and EOI
 265 scenarios and the corresponding cardinality of P_k are presented in Fig. 3. We intentionally do not present the SSK
 266 scenario plot as it involves a single position in the 3D space rather than a trajectory. In the SSK scenario P_k
 267 constantly comprises of 4556 vertices.
 268
 269

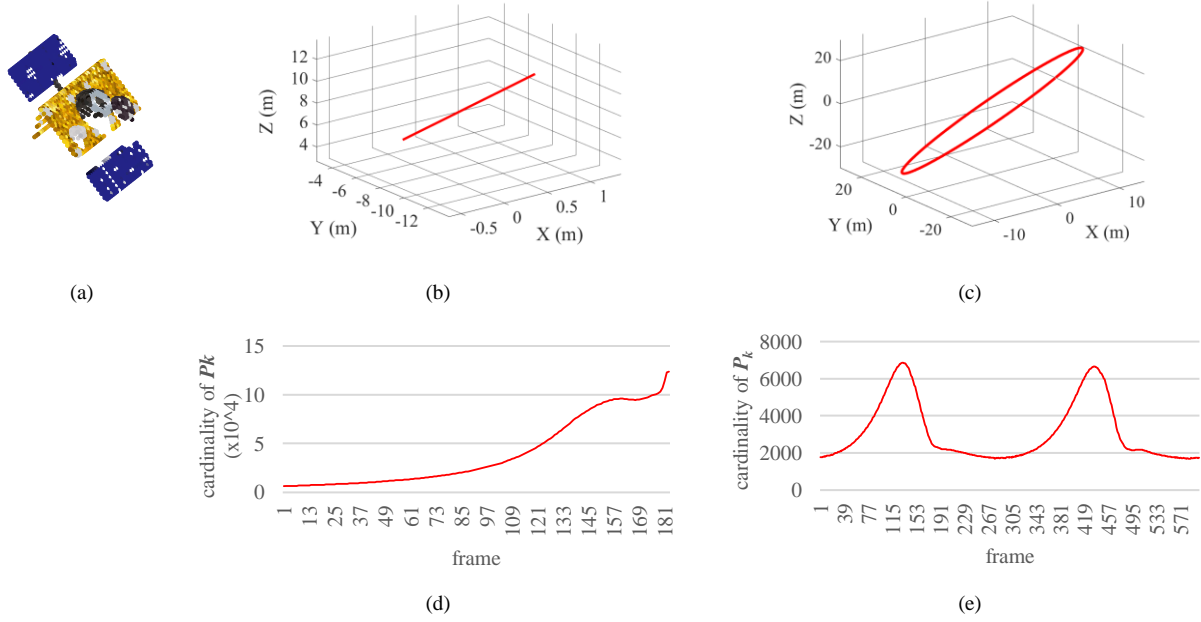


Fig. 3. (a) Target platform, trajectory plot of the (b) SLA trajectory (c) EOI trajectory and *Target* point cloud cardinality for the (d) SLA trajectory and (e) EOI trajectory

270

271

272

273

274

275

276

277

278

In the following trials, we compare the suggested architecture against current space oriented architectures and specifically against OUR-CV FH combined with ICP [28], Spin Images combined with ICP [28] and ICP only [9,16,17,26,27] with pose initialization considered as given. The parameters of the architecture and of the competing methods are tuned based on the SLA Scenario. Table 2 presents the tuned parameters, while the ones not tuned are fixed either to the ones originally proposed by their authors or for OUR-CV FH and Spin Images to their PCL implementation [34,49,50]. Odometry performance is evaluated based on drift, i.e. RMSE between the estimated end-point and the ground truth (GT) end-point, T_{error} presenting the overall translational error as a percentage over the GT distance travelled, average and maximum translational error per axis, rotational error, and processing time.

Table 2.
Tuned parameters

Module	Tuned parameters
q_r quantization factor	15
FH keypoint detector	6 scale levels / blob threshold 10^{-5}
GFTT keypoint detector	Min. corner quality 10^{-3} / Gaussian filter size 3x3
Correspondence grouping	$\epsilon = 200$ times the P_{k+1} resolution / minimum cluster size 10
Kalman filtering	$\sigma_v = 1$ / $\sigma_w = 5 \cdot 10^{-3}$ / number of iterations equal to the cardinality of Ω
H_∞ filtering	$dt = 10^{-5}$ / $g = 0.1$ / number of iterations equal to the cardinality of Ω
OUR-CV FH	5° angular threshold / curvature threshold 1, axis ratio 0.8
Spin Images	description radius 0.02 / 8 resolution bins
ICP	point-to-point variant / 1% translational tolerance / max iterations 1000
Cardinality threshold	3

279 3.2 Odometry trials

280 3.2.1 SLA Scenario

281 This is a constant *Target* pose scenario where the *Source* – *Target* range is decreasing, simulating the
282 approaching phase of the *Source* towards the *Target* platform. Most accurate odometry is provided by the GFTT
283 keypoint detector combined with the KAZE feature descriptor regardless of the recursive filtering method used.
284 Indeed, the GFTT / KAZE combined with Kalman attains 0.354m drift (1.598% translational error) and if combined
285 with H_∞ it provides 0.355m (1.602%). Lowest accuracy is **delivered** by the FH / FREAK and FH / BRISK
286 combinations, regardless of the recursive filtering method used. This is because neither of the binary descriptors
287 provide adequate feature matches and therefore at most *Target* pose instances our algorithm preserves the
288 initialization value $R = R_0^*$, imposing the FH / FREAK and FH / BRISK combinations to be constrained close to the
289 initial X, Y, Z coordinates of this trial. The low number of feature matches attained by both binary descriptors
290 confirms [51]. Interestingly, both recursive filtering methods provide similar results when combined with the same
291 keypoint detection and feature description method, highlighting the importance of selecting a robust keypoint
292 detection and feature description combination. Table 3 presents the performance metrics on the SLA scenario, while
293 Fig. 4 illustrates the corresponding odometry trajectories.

294 In terms of rotational accuracy, all combinations perform equally well attaining very low errors for Kalman and
295 H_∞ filtering, which are in the order of 10^{-8} and 10^{-3} °/m, respectively. One of the major contributions of the
296 proposed architecture is the very low processing time required. Indeed, the computational burden of each method is
297 in the order of milliseconds **validating the capability of the suggested odometry architecture** to fully exploit the low
298 processing cost of the 2D keypoint detection and feature description methods. It should be noted that processing
299 time includes not only the keypoint detection, feature description, geometric consistency checks and recursive
300 filtering processes, but also the 3D to multi-2.5D remapping and the multi-2.5D to 3D back-projection processes.

301 Compared to the competitor odometry solutions evaluated in this paper, the proposed architecture in most
302 combinations attains at least one order of magnitude better performance in all metrics. An exception is only the
303 processing time of ICP, which is only 40 milliseconds faster compared to the fastest combination of the proposed
304 architecture. However, the translational and the rotational error provided by ICP are much higher compared to any
305 combinations of the architecture suggested. In fact, even though the LIDAR point cloud acquisition rate is large
306 **enough to provide a small frame-to-frame *Target* pose change, yet ICP still fails** to properly register the two

307 successive point clouds. Regarding OUR-CVFH / ICP, it lacks an appealing performance because it fails to cluster
308 the *Target*'s surfaces and thus it considers the entire *Target* as a single cluster and automatically degrades to the less
309 accurate VFH technique. Main reason for OUR-CVFH failing to cluster the *Target* platform is the relative pose of
310 the latter as observed by the LIDAR sensor in combination with the varying *Source* – *Target* distance, forcing the
311 *Target* platform to comprise of connected flat surfaces at most instances. Spin Images / ICP also lack of a high
312 performance due to the symmetric and mostly flat surfaces of the *Target* platform affecting the descriptiveness and
313 robustness of the Spin Image feature descriptor. The rotational error of all competitor methods is approximately 2.6
314 degrees per meter ($^{\circ}/m$), indicating that ICP, which is the common module of all three techniques evaluated has a
315 great impact on the rotational error. In terms of computational burden, ICP and OUR-CVFH/ ICP have a processing
316 burden in the order of milliseconds. In contrast, Spin Images with ICP require the highest processing time among all
317 methods evaluated including the suggested architecture. This is because, in current literature [28], Spin Images is not
318 combined with a 3D keypoint detector and thus all *Target* vertices are encoded. Additionally, Spin Images is a 3D
319 local description method which requires establishing a reference axis for each described keypoint, imposing an
320 additional processing burden.

321 From Table 3 it is evident that the suggested architecture, apart from the FH / FREAK and FH / BRISK, is
322 considerably more accurate than any competitor technique. The proposed architecture is both accurate and
323 computationally efficient for the following reasons; first, it employs 2D keypoint detection and description methods
324 that are unarguably robust to minor scale and rotational changes that are present in the point cloud projections of
325 sequential *Target* pose instances, second, recursive filtering is designed for robustness against noise and outliers,
326 and third, the 2D methods employed are considerably faster to execute compared to their 3D counterparts [35].

327

328

329

330

331

332

333

334

Table 3.
Performance metrics for the SLA scenario (Top performance is highlighted in bold)

	drift (m)	T_{error} (%)	Max error (m)			Average error (m)			Rotational error (°/m)	Processing time (s)
			X	Y	Z	X	Y	Z		
Kalman recursive filtering										
FH / SURF	1.151	5.183	0.954	1.248	0.231	0.285	0.420	0.103	3.99 10⁻⁸	0.281
FH / FREAK	14.969	67.419	0.055	10.608	10.561	0.035	5.371	5.335	2.36 10 ⁻⁸	0.374
FH / BRISK	15.504	69.828	0.014	10.960	10.966	0.004	5.511	5.513	2.36 10 ⁻⁸	0.801
FH / KAZE	0.735	3.312	0.674	0.969	0.231	0.103	0.237	0.103	3.99 10⁻⁸	0.286
GFTT / SURF	0.482	2.175	0.476	0.790	0.246	0.079	0.215	0.113	1.77 10 ⁻⁵	0.355
GFTT / FREAK	1.636	7.372	1.106	1.400	0.643	0.384	0.532	0.112	2.36 10 ⁻⁸	0.395
GFTT / BRISK	1.316	5.928	0.501	0.939	0.921	0.094	0.246	0.186	2.36 10 ⁻⁸	0.741
GFTT / KAZE	0.354	1.598	0.431	0.446	0.246	0.244	0.117	0.112	1.49 10 ⁻⁸	0.363
H∞ recursive filtering										
FH / SURF	1.134	5.109	0.943	1.240	0.219	0.278	0.415	0.095	0.005	0.281
FH / FREAK	14.968	67.413	0.055	10.607	10.560	0.035	5.370	5.334	0.001	0.374
FH / BRISK	15.504	69.827	0.014	10.960	10.966	0.004	5.511	5.513	0.001	0.801
FH / KAZE	0.717	3.233	0.663	0.960	0.219	0.097	0.231	0.095	0.005	0.286
GFTT / SURF	0.472	2.127	0.466	0.790	0.236	0.075	0.215	0.106	0.005	0.357
GFTT / FREAK	1.616	7.279	1.095	1.388	0.631	0.377	0.524	0.104	0.004	0.395
GFTT / BRISK	1.299	5.851	0.490	0.927	0.909	0.095	0.239	0.179	0.004	0.741
GFTT / KAZE	0.355	1.602	0.441	0.445	0.236	0.251	0.117	0.105	0.005	0.364
competitor schemes										
ICP	5.629	25.352	2.981	3.326	3.685	1.703	1.542	2.071	2.609	0.239
OUR-CVfH / ICP	5.631	25.361	10.541	10.857	36.903	2.699	2.789	6.618	2.620	0.953
Spin Images / ICP	5.631	25.361	16.402	16.537	69.554	6.839	6.976	24.229	2.620	391.312

335

336 3.2.2 EOI Scenario

337 This scenario considers a frame-to-frame varying *Target* pose at a fixed *Source* – *Target* distance, simulating the
338 *Source* platform orbiting around the *Target* platform. For the proposed odometry technique, the hierarchy of the top
339 performing combinations is maintained with the GFTT / KAZE achieving 0.947m drift (0.325%). Similar to
340 scenario one, both recursive filtering methods provide an equally accurate odometry trajectory. Regarding the
341 rotational error, all methods under both recursive filtering schemes perform equally well attaining a small error in
342 the order of 10⁻³ °/m. In contrast to the SLA scenario, the majority of methods evaluated afford a considerably
343 smaller processing burden and this is because of the point cloud cardinality of the *Target* platform which in this trial
344 is much smaller compared to the SLA scenario. Table 4 presents the performance metrics on the EOI scenario, while
345 Fig. 5 illustrates the corresponding odometry trajectories.

346 Also, in terms of translational and rotational error, the competitor methods attain an inferior performance
347 compared to the suggested architecture. An exception is the processing requirement that is of the same order
348 compared to the solution presented in this work.

349

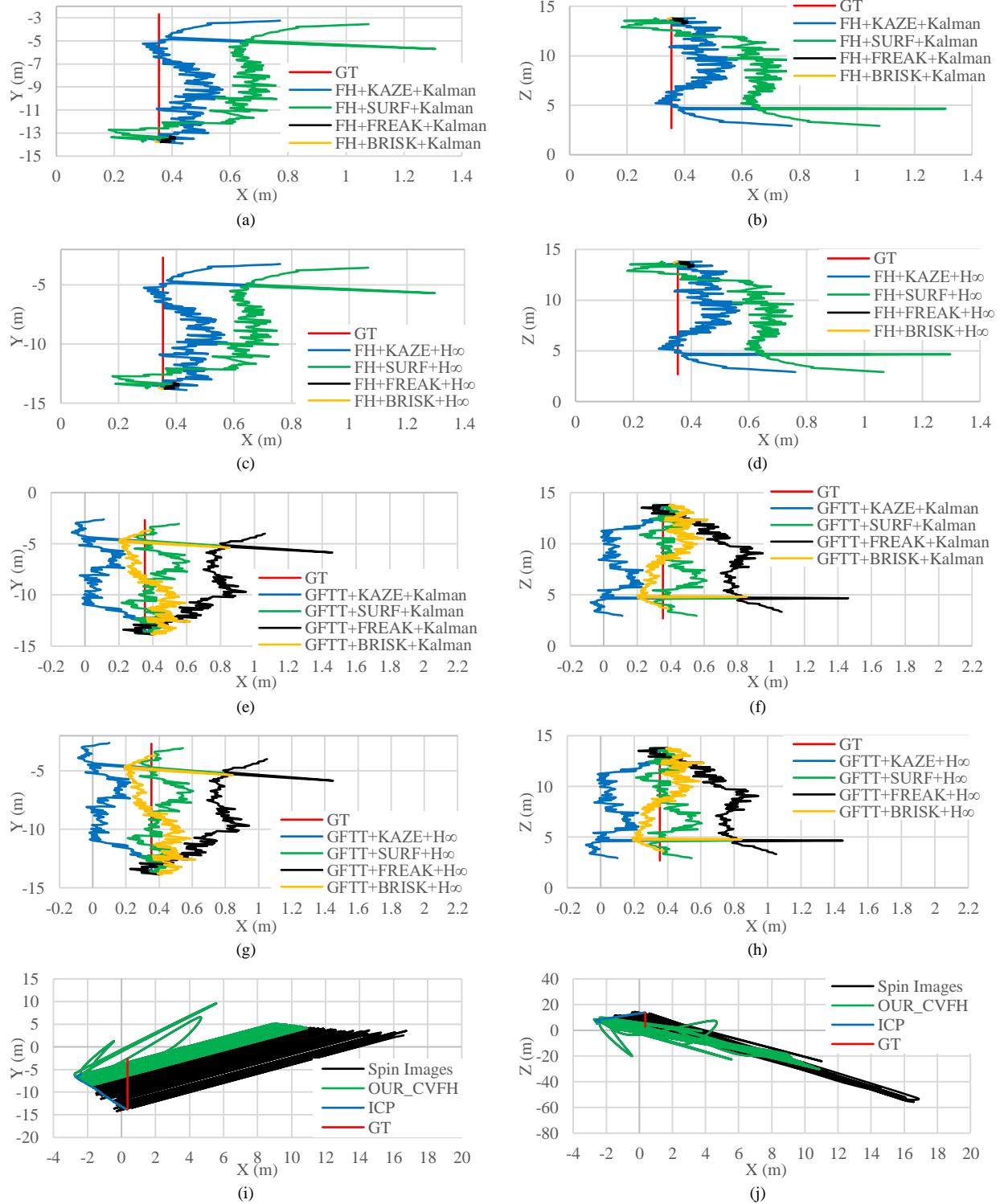


Fig. 4. 2D odometry plots for the SLA scenario (a)-(h) proposed architecture under various configurations, (i)-(j) competitor odometry methods

350

351

352

Table 4.
Performance metrics for the EOI scenario (Top performance is highlighted in bold)

	drift (m)	T_{error} (%)	Max error (m)			Average error (m)			Rotational error (°/m)	Processing time (s)
			X	Y	Z	X	Y	Z		
Kalman recursive filtering										
FH / SURF	2.601	0.892	3.013	4.414	1.067	1.164	1.026	0.496	0.002	0.053
FH / FREAK	9.241	3.171	15.521	47.039	51.061	9.0726	22.479	23.667	0.002	0.128
FH / BRISK	1.577	0.541	14.096	55.732	56.893	8.544	27.162	27.73	0.002	0.482
FH / KAZE	2.298	0.788	3.129	1.823	1.068	1.062	0.641	0.364	0.002	0.057
GFTT / SURF	1.486	0.509	2.462	1.649	1.229	0.740	0.696	0.505	0.002	0.096
GFTT / FREAK	3.079	1.056	3.440	4.412	2.964	0.8032	0.9022	0.797	0.002	0.122
GFTT / BRISK	4.607	1.581	6.694	6.242	3.501	1.983	1.718	1.990	0.002	0.481
GFTT / KAZE	0.947	0.325	2.500	2.454	0.918	0.566	1.085	0.390	0.002	0.094
H_{∞} recursive filtering										
FH / SURF	2.639	0.905	2.995	4.455	1.025	1.161	1.033	0.484	0.003	0.053
FH / FREAK	9.254	3.175	15.512	47.030	51.053	9.070	22.475	23.660	0.002	0.128
FH / BRISK	1.581	0.542	14.097	55.731	56.891	8.543	27.161	27.729	0.002	0.481
FH / KAZE	2.306	0.791	3.111	1.780	1.060	1.057	0.630	0.360	0.003	0.058
GFTT / SURF	1.532	0.525	2.444	1.601	1.150	0.740	0.708	0.468	0.003	0.098
GFTT / FREAK	3.085	1.058	3.421	4.466	2.665	0.806	0.901	0.792	0.003	0.123
GFTT / BRISK	4.605	1.580	6.725	6.236	3.496	1.994	1.705	1.998	0.002	0.481
GFTT / KAZE	0.909	0.312	2.500	2.401	0.822	0.568	1.059	0.371	0.003	0.095
competitor schemes										
ICP	50.320	17.266	35.619	9.370	59.270	12.575	3.752	29.812	0.199	0.030
OUR-CVFH / ICP	50.312	17.263	35.667	9.199	58.965	12.557	3.755	29.744	0.200	0.163
Spin Images / ICP	35.661	12.236	53.077	102.206	183.474	13.926	8.599	36.730	0.148	0.672

353

354 3.2.3 SSK Scenario

355 This scenario simulates the case where the *Source* platform is relatively stationary against the *Target* platform.

356 Even though this can be considered as a low complexity scenario, it nevertheless is the last part of a complete space

357 trajectory and therefore we investigate it. Table 5 presents the performance metrics on the SSK scenario. Regarding

358 the proposed odometry technique, all evaluated combinations attain a very low drift. Even though both binary

359 descriptors, i.e. FREAK and BRISK, combined with any of the keypoint detectors and recursive filtering methods

360 evaluated achieve zero drift, the results for these two descriptors are ostensive. This is because for the *Source* –

361 *Target* distance examined in this scenario, both binary descriptors do not manage to provide any feature **matches**.

362 Therefore, the suggested pipeline (Fig. 2) inputs the initialization value $R = R_0^*$ to Eq. (1), and thus ultimately it

363 remains at the initial X, Y, Z position. In terms of processing efficiency, all combinations attain a low execution time.

364 For this scenario, ICP also presents an appealing option providing only a small drift and a low computational

365 burden. **Although** OUR-CVFH/ ICP provides a low drift, it imposes a quite high computational burden neglecting it

366 from an appealing near-real-time solution. Finally, despite the combination of Spin Images with ICP being highly

367 accurate, it has an extremely high processing requirement neglecting it from an optimum odometry solution.

368 It should be noted that, in any case, since the ground-truth translation between the initial and the end-point of the

369 *Source* platform position coincide, T_{error} and rotational error per meter travelled metrics are not applicable.

370

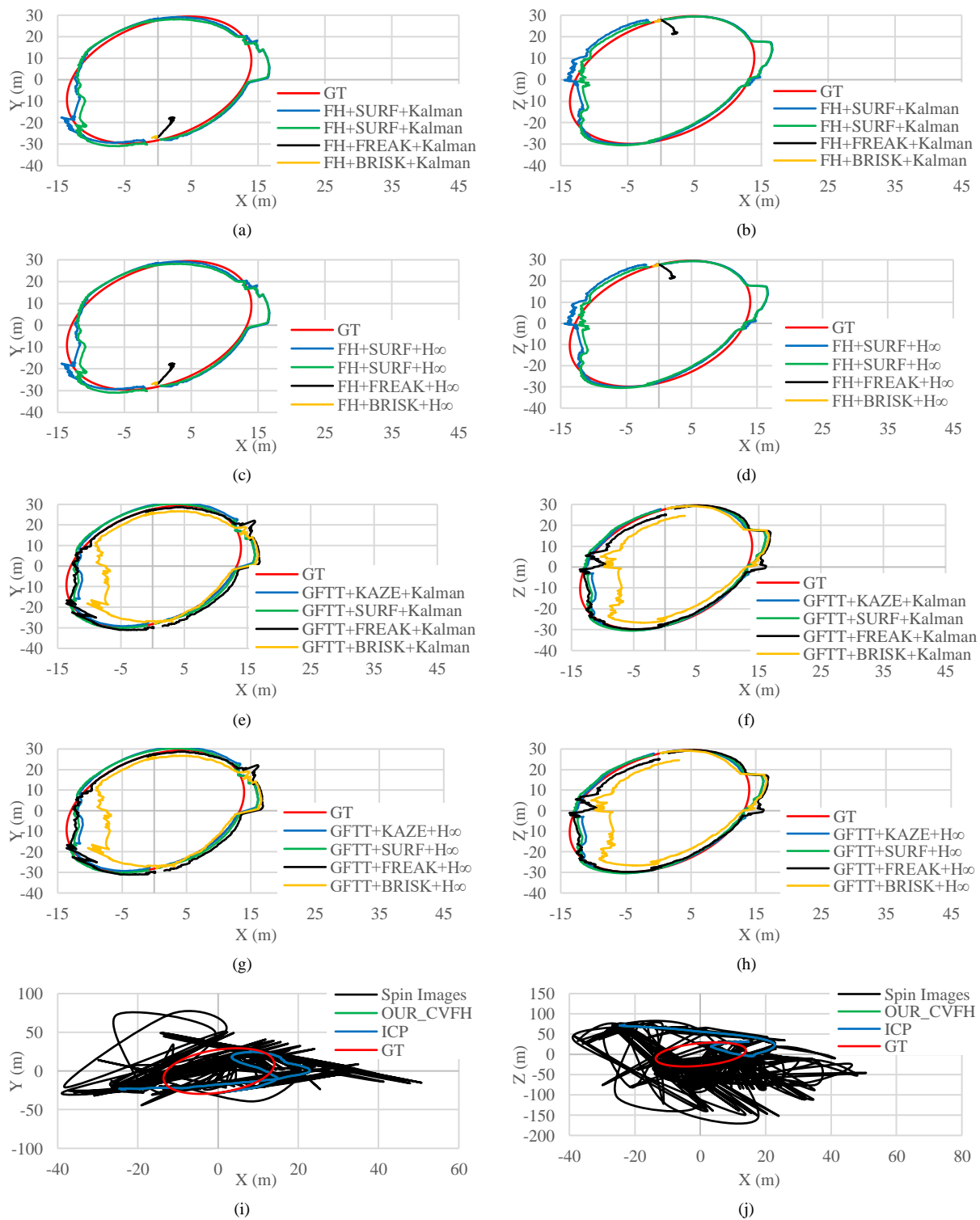


Fig. 5. 2D odometry plots for the EOI scenario (a)-(h) proposed architecture under various configurations, (i)-(j) competitor odometry methods

371

372

373

Table 5.
Performance metrics for the SSK scenario

	drift (m)	T_{error} (%)	Max error (m)			Average error (m)			Rotational error ($^{\circ}$ /m)	Processing time (s)
			X	Y	Z	X	Y	Z		
Kalman recursive filtering										
FH / SURF	$6 \cdot 10^{-3}$	-	$5 \cdot 10^{-3}$	$3 \cdot 10^{-3}$	$5 \cdot 10^{-4}$	10^{-3}	$8 \cdot 10^{-4}$	10^{-4}	-	0.817
FH / FREAK	0	-	0	0	0	0	0	0	-	1.125
FH / BRISK	0	-	$2 \cdot 10^{-9}$	10^{-8}	10^{-8}	$2 \cdot 10^{-9}$	10^{-8}	10^{-8}	-	1.205
FH / KAZE	10^{-8}	-	$2 \cdot 10^{-9}$	10^{-8}	10^{-8}	$2 \cdot 10^{-9}$	10^{-8}	10^{-8}	-	0.893
GFTT / SURF	$6 \cdot 10^{-6}$	-	10^{-6}	10^{-8}	$6 \cdot 10^{-6}$	$7 \cdot 10^{-7}$	10^{-8}	$3 \cdot 10^{-6}$	-	0.855
GFTT / FREAK	10^{-8}	-	$2 \cdot 10^{-9}$	10^{-8}	10^{-8}	$2 \cdot 10^{-9}$	10^{-8}	10^{-8}	-	0.948
GFTT / BRISK	10^{-8}	-	0	0	0	0	0	0	-	1.274
GFTT / KAZE	$6 \cdot 10^{-6}$	-	$2 \cdot 10^{-9}$	10^{-8}	$6 \cdot 10^{-5}$	$2 \cdot 10^{-9}$	10^{-8}	$3 \cdot 10^{-6}$	-	0.886
H_{∞} recursive filtering										
FH / SURF	$6 \cdot 10^{-3}$	-	$5 \cdot 10^{-3}$	$3 \cdot 10^{-3}$	$5 \cdot 10^{-4}$	10^{-3}	$9 \cdot 10^{-4}$	10^{-4}	-	0.817
FH / FREAK	0	-	0	0	0	0	0	0	-	1.120
FH / BRISK	0	-	$4 \cdot 10^{-5}$	$7 \cdot 10^{-4}$	$2 \cdot 10^{-5}$	$2 \cdot 10^{-5}$	$3 \cdot 10^{-4}$	10^{-5}	-	1.201
FH / KAZE	$7 \cdot 10^{-4}$	-	$9 \cdot 10^{-5}$	$7 \cdot 10^{-4}$	10^{-5}	$2 \cdot 10^{-5}$	$3 \cdot 10^{-4}$	$6 \cdot 10^{-6}$	-	0.893
GFTT / SURF	$7 \cdot 10^{-4}$	-	$4 \cdot 10^{-5}$	$7 \cdot 10^{-4}$	$4 \cdot 10^{-5}$	$2 \cdot 10^{-5}$	$3 \cdot 10^{-4}$	$2 \cdot 10^{-5}$	-	0.856
GFTT / FREAK	$7 \cdot 10^{-4}$	-	$4 \cdot 10^{-5}$	$7 \cdot 10^{-4}$	$2 \cdot 10^{-5}$	$2 \cdot 10^{-5}$	$3 \cdot 10^{-4}$	10^{-5}	-	0.948
GFTT / BRISK	$7 \cdot 10^{-4}$	-	0	0	0	0	0	0	-	1.274
GFTT / KAZE	$7 \cdot 10^{-4}$	-	$4 \cdot 10^{-5}$	$7 \cdot 10^{-4}$	10^{-5}	$2 \cdot 10^{-5}$	$3 \cdot 10^{-4}$	$9 \cdot 10^{-6}$	-	0.887
competitor schemes										
ICP	$7 \cdot 10^{-6}$	-	$4 \cdot 10^{-6}$	10^{-8}	$6 \cdot 10^{-6}$	$2 \cdot 10^{-6}$	10^{-8}	$3 \cdot 10^{-6}$	-	0.283
OUR-CVFH / ICP	$4 \cdot 10^{-6}$	-	$4 \cdot 10^{-6}$	$2 \cdot 10^{-7}$	$4 \cdot 10^{-6}$	10^{-6}	$2 \cdot 10^{-7}$	10^{-6}	-	33.242
Spin Images / ICP	0	-	0	0	0	0	0	0	-	2700.00

374

375 3.3 Discussion

376 In Section 3, for each scenario we present the overall performance of several keypoint detection, feature
377 description, and recursive filtering combinations. Therefore, for a more comprehensive analysis, Table 6 presents
378 the overall performance attained by each scheme on an individual basis, e.g. overall performance of each keypoint
379 detection method **independent** of the feature description and recursive filtering method.

380 From the results presented in Table 6, it can be concluded that GFTT keypoints contribute to a more accurate
381 odometry solution. This is because when the point cloud is remapped from the 3D to the 2D space, the number of
382 corners detected by GFTT are more compared to the blob-type keypoints detected by FH. This performance is
383 highly related to the quantization factor of Eq. (5) because it defines the level of details that each projection
384 encloses. However, since in this work odometry accuracy and processing efficiency are of equal importance, we
385 choose a relatively small q_f value that affords high-speed odometry but favours the corner type detectors.
386 Increasing q_f creates sparse 2.5D projections negatively influencing the performance of the 2D keypoint detection
387 and feature description methods employed. Reducing q_f on the other hand prohibits the 2D keypoint detectors from
388 providing repeatable keypoints. Finally, in terms of rotational error and computational requirements, both keypoint
389 detection methods attain similar results.

390 Considering the performance of the feature description methods, KAZE and SURF are the most appealing ones
391 attaining lowest drift at a **relatively low computational cost**, which is one of the lowest presented in our experiments.
392 Their performance is similar because both descriptors belong to the same category, i.e. floating-point, and share the
393 same description method, i.e. Gaussian-weighted Haar wavelet responses, with the difference being that SURF has a
394 linear and KAZE a non-linear scale-space description scheme. Due to this difference, KAZE affords a lower drift
395 but also a mildly larger processing requirement. Similarly, BRISK and FREAK achieve similar results as both are
396 binary and rely on a sampling pattern comprising of concentric circular patches centred at a keypoint. Their
397 difference is that BRISK has a constant sampling point density, while FREAK has a variable one with the sampling
398 points being denser near the centre **becoming** exponentially less dense further away from the centre. However, in the
399 context of multi-projecting point clouds, this variable sampling point density does not provide any performance gain
400 to FREAK. In fact, the fixed sampling pattern of both binary techniques does not encode the keypoints detected on
401 the 2.5D projection images robustly, and thus it can be concluded that these descriptors are less suitable for 2.5D
402 imagery. Finally, from Table 6 we conclude that given the keypoint detection and feature description **method's**
403 **capability to** provide good matches, the selection of the recursive filtering method **remains** less important. Indeed,
404 the overall performance of the two recursive methods evaluated is very similar for the scenarios of this work.
405

Table 6.
Performance analysis (Top performance is highlighted in bold)

module	method	drift (m)	T_{error} (%)	Rotational error ($^{\circ}/\text{m}$)	Processing time (s)
Keypoint detection	FH	4.008	18.884	$1.66 \cdot 10^{-3}$	0.422
	GFTT	1.158	2.555	$2.37 \cdot 10^{-3}$	0.552
Feature description	SURF	0.960	2.179	$2.42 \cdot 10^{-3}$	0.410
	FREAK	4.821	19.743	$1.64 \cdot 10^{-3}$	0.370
	BRISK	3.833	19.460	$1.59 \cdot 10^{-3}$	0.737
	KAZE	0.719	1.495	$2.42 \cdot 10^{-3}$	0.431
Filtering method	Kalman	2.583	10.730	$8.97 \cdot 10^{-4}$	0.487
	H_{∞}	2.583	10.730	$3.14 \cdot 10^{-3}$	0.487

406

407 **We also assess the interplay between the feature matching and the geometric consistency checks (GCC) module**
408 **of our odometry architecture by discarding the latter and setting to eq. (12) a fixed threshold of 0.8 [38,52]. For**
409 **better readability we only assess the SLA scenario, with the corresponding results presented in Table 7. Our findings**
410 **demonstrate that the top performing combination utilizing the GFTT keypoint detector with the KAZE feature**
411 **descriptor, indeed benefits from using the GCC, with the translational improvement being approximately 55% for**

412 both recursive filtering schemes, i.e. Kalman and $H\infty$. In terms of rotation, utilizing a GCC has a minor impact that
413 is less than 1% and regarding computational efficiency, the GCC imposes an additional 26% processing time.
414 However, as presented in Table 3, the total computational burden including the GCC module is only 363ms and thus
415 the extra 95ms required by the GCC module are considered as minor drawback.

416 In Table 7 we also demonstrate that the keypoint detection and feature description methods have a great interplay
417 with the GCC module. In fact, we show that when GFFT is combined with GCC, it attains a translational
418 performance gain regardless of the feature descriptor and recursive filtering scheme used, while the impact on the
419 rotational error is minor. Accordingly, SURF is the most affected descriptor with BRISK to follow. On the contrary,
420 the FH keypoint detector is more robust and thus, depending on the feature descriptor that SURF is combined with,
421 neglecting the GCC module may have a greater impact. This is because the *Target* has a frame-to-frame 3D rotation
422 imposing some of the keypoints detected on the 2.5D images being transferred from the background to the
423 foreground and vice versa leading to a local zooming effect [53]. Given that GFFT is prone to scale changes and to
424 affine transformations, the frame-to-frame keypoints detected in all 2.5D projections include both true and false
425 matching correspondences affecting accordingly the performance of the feature descriptor. However, the GCC
426 module evaluates the geometric consistency of the correspondences discarding the majority of the false matches and
427 ultimately provides an appealing odometry. On the contrary, FH is robust to scale changes and to out-of-plane
428 *Target* rotations of up to 30° affording a great number of true matching and fewer false matching correspondences.
429 Hence the strict threshold within the GCC module force true matching correspondences to be discarded, reducing
430 the number of iterations of the recursive filter and thus imposing it not to properly settle. In simple terms, GFFT
431 provides one order of magnitude more keypoints than FH, where only a few of these keypoints are true matching
432 correspondences and GCC assists into discarding the false matching ones. However, it should be noted that FH/
433 SURF, which is the most accurate combination among the ones relying on FH when a GCC scheme is neglected, is
434 still inferior to the GFFT/KAZE that uses a GCC module.

435

436

437

438

439

Table 7.

Performance assessment on the SLA scenario neglecting correspondence grouping (all metrics in %, positive refers to performance gain by using correspondence grouping and negative refers to loss)

	drift	T _{error}	Rotational error	Processing time	drift	T _{error}	Rotational error	Processing time
	Kalman recursive filtering				H_∞ recursive filtering			
FH / SURF	-5.26	-5.26	-40.76	-9.65	-4.73	-4.73	-0.99	-9.67
FH / FREAK	-0.18	-0.18	0.00	-36.22	-0.18	-0.18	0.16	-36.26
FH / BRISK	0.05	0.05	0.00	-8.05	0.05	0.05	0.66	-8.06
FH / KAZE	-14.56	-14.56	-40.76	-14.80	-15.03	-15.03	-0.12	-14.83
GFTT / SURF	115.32	115.32	-0.87	-23.92	117.96	117.96	0.76	-23.97
GFTT / FREAK	50.53	50.53	0.00	-32.78	51.48	51.48	-1.84	-32.79
GFTT / BRISK	83.81	83.81	0.00	-15.39	85.40	85.40	-1.89	-15.40
GFTT / KAZE	54.89	54.89	-0.84	-26.22	55.70	55.70	0.08	-26.28

440

441 For completeness, it is worth noting that although the suggested architecture presents an overall appealing
 442 odometry performance, it poses the following limitations:

443 a. The quantization factor q_f has to be tuned based on the *Target* point cloud resolution. Properly tuning q_f
 444 is important as it defines the 3D to multi-2D remapping and ultimately affects the performance of the 2D keypoint
 445 detectors and descriptors, and thus the accuracy of the proposed odometry architecture. However, tuning q_f is done
 446 offline neglecting any impact during the odometry process.

447 b. *Target* tumbling should not exceed the robustness of the 2D method's used affine transformation. This is
 448 the case where the *Target* undergoes a 3D rotation creating on at least one of the 2.5D projection planes a large out-
 449 of-plane projection. This is due to the XYZ_{LIDAR} reference frame and the translated XYZ_{Target} reference frame having
 450 axes that are fixed on the LIDAR sensor onboard the *Source*. However, this is only for the case where parts of the
 451 *Target* have not shifted yet from one 2.5D projection plane to another and thus remain on the same 2.5D plane but
 452 under a large affine transformation.

453

454 4. Conclusion

455 LIDAR based odometry for space relative navigation is a challenging task. Given the cost and the importance of
 456 space missions, highly accurate and processing efficient odometry becomes mandatory. Driven by these
 457 requirements and the performance of current methods, we propose a high-speed and robust LIDAR based odometry
 458 architecture appropriate for space odometry that combines the advantages of the 3D and 2D data domains along with
 459 the robustness of recursive filtering. Specifically, our architecture attains a high odometry accuracy by exploiting the
 460 advantages of 3D LIDAR data and recursive filtering, while in parallel it achieves a low computational burden by

461 transforming the odometry problem from the 3D space into multiple 2D ones that involve 2.5D image projections of
462 the 3D data.

463 Trials evaluate several current state-of-the-art 2D keypoint detection, local feature description and recursive
464 filtering techniques on several simulated scenarios that involve a realistic *Target* space platform. Results
465 demonstrate that the proposed architecture affords higher odometry accuracy and a lower processing burden
466 compared to current methods. Specifically, **highest performance is gained by the GFTT/ KAZE combination that**
467 **manages one order of magnitude more accurate odometry and a very low processing burden, which depending on**
468 **the competitor method, may exceed one order of magnitude faster odometry computation. Spurred by the appealing**
469 **performance of the proposed architecture, future work shall include implementation on space-graded FPGA boards**
470 **and extended to provide pose initialization.**

471

472 **Conflict of interest statement**

473 None declared

474 **Funding Sources**

475 This research was supported by the European Union’s Horizon 2020 research and innovation program, under
476 project “Integrated 3D Sensors (I3DS)” with grant agreement No 730118.

477 **Acknowledgements**

478 The authors would like to thank Thales Alenia Space (France) for providing simulated data.

479 **References**

- 480 [1] M.S. Krämer, S. Hardt, K. Kuhnert, Image Features in Space - Evaluation of Feature Algorithms for Motion Estimation in Space
481 Scenarios, in: Proc. 7th Int. Conf. Pattern Recognit. Appl. Methods, SCITEPRESS - Science and Technology Publications, Funchal,
482 Madeira, Portugal, 2018: pp. 300–308. doi:10.5220/0006555303000308.
- 483 [2] D. Rondao, N. Aouf, Multi-View Monocular Pose Estimation for Spacecraft Relative Navigation, 2018 AIAA Guid. Navig. Control
484 Conf. (2018). doi:10.2514/6.2018-2100.
- 485 [3] L. Li, J. Lian, L. Guo, R. Wang, Visual odometry for planetary exploration rovers in sandy terrains, Int. J. Adv. Robot. Syst. 10 (2013)
486 1–7. doi:10.5772/56342.
- 487 [4] T. Tykkala, A.I. Comport, A dense structure model for image based stereo SLAM, in: Robot. Autom. (ICRA), 2011 IEEE Int. Conf.,

488 Shanghai, China, 2011: pp. 1758–1763. doi:10.1109/ICRA.2011.5979805.

489 [5] Yang Cheng, M. Maimone, L. Matthies, Visual Odometry on the Mars Exploration Rovers, in: 2005 IEEE Int. Conf. Syst. Man
490 Cybern., Waikoloa, HI, USA, 2006: pp. 903–910. doi:10.1109/ICSMC.2005.1571261.

491 [6] M. Maimone, Y. Cheng, L. Matthies, Two years of Visual Odometry on the Mars Exploration Rovers, *J. F. Robot.* 24 (2007) 169–186.
492 doi:10.1002/rob.20184.

493 [7] O. Yılmaz, N. Aouf, L. Majewski, M. Sanchez-Gestido, G. Ortega, Using infrared based relative navigation for active debris removal,
494 in: 10th Int. ESA Conf. Guid. Navig. Control Syst., Salzburg, Austria, 2017: pp. 1–16.

495 [8] B. Naasz, M. Moreau, Autonomous RPOD technology challenges for the coming decade, *Adv. Astronaut. Sci.* 144 (2012) 403–425.

496 [9] R. Opromolla, M.Z. Di Fraia, G. Fasano, G. Rufino, M. Grassi, Laboratory test of pose determination algorithms for uncooperative
497 spacecraft, in: 4th IEEE Int. Work. Metrol. AeroSpace, Metroaerosp. 2017 - Proc., Padua, Italy, 2017: pp. 169–174.
498 doi:10.1109/MetroAeroSpace.2017.7999558.

499 [10] J.O. Woods, J.A. Christian, Lidar-based relative navigation with respect to non-cooperative objects, *Acta Astronaut.* 126 (2016) 298–
500 311. doi:10.1016/j.actaastro.2016.05.007.

501 [11] R. Volpe, G. Palmerini, M. Sabatini, Monocular and Lidar Based Determination of Shape , Relative Attitude and Position of a Non-
502 Cooperative , Unknown Satellite, in: *Int. Astronaut. Congr. (IAC 2017)*, Adelaide, Australia, 2017: pp. 25–29.

503 [12] H. Gómez Martínez, G. Giorgi, B. Eissfeller, Pose estimation and tracking of non-cooperative rocket bodies using Time-of-Flight
504 cameras, *Acta Astronaut.* 139 (2017) 165–175. doi:10.1016/j.actaastro.2017.07.002.

505 [13] J. Galante, J. Van Eepoel, M. Strube, N. Gill, M. Gonzalez, A. Hyslop, B. Patrick, Pose Measurement Performance of the Argon
506 Relative Navigation Sensor Suite in Simulated-Flight Conditions, in: *AIAA Guid. Navig. Control Conf.*, American Institute of
507 Aeronautics and Astronautics, Reston, Virginia, 2012: pp. 1–26. doi:10.2514/6.2012-4927.

508 [14] J.L. Sell, A. Rhodes, J.O. Woods, J.A. Christian, T. Evans, Pose Performance of LIDAR-Based Navigation for Satellite Servicing,
509 *AIAA/AAS Astrodyn. Spec. Conf.* (2014) 1–14. doi:10.2514/6.2014-4360.

510 [15] J. Song, Sliding window filter based unknown object pose estimation, in: 2017 IEEE Int. Conf. Image Process., IEEE, 2017: pp. 2642–
511 2646. doi:10.1109/ICIP.2017.8296761.

512 [16] R. Opromolla, G. Fasano, G. Rufino, M. Grassi, Spaceborne LIDAR-based system for pose determination of uncooperative targets, in:
513 2014 IEEE Int. Work. Metrol. Aerospace, Metroaerosp. 2014 - Proc., Benevento, Italy, 2014: pp. 265–270.
514 doi:10.1109/MetroAeroSpace.2014.6865932.

515 [17] R. Opromolla, G. Fasano, G. Rufino, M. Grassi, A model-based 3D template matching technique for pose acquisition of an
516 uncooperative space object, *Sensors (Switzerland)*. 15 (2015) 6360–6382. doi:10.3390/s150306360.

517 [18] O. Kechagias-stamatis, N. Aouf, H_{∞} LIDAR Odometry for Spacecraft Relative Navigation, *IET Radar, Sonar Navig.* (2019).
518 doi:10.1049/iet-rsn.2018.5354.

519 [19] R. Opromolla, G. Fasano, G. Rufino, M. Grassi, A review of cooperative and uncooperative spacecraft pose determination techniques
520 for close-proximity operations, *Prog. Aerosp. Sci.* 93 (2017) 53–72. doi:10.1016/j.paerosci.2017.07.001.

521 [20] M. Zarei-Jalalabadi, S.M.-B. Malaek, Motion estimation of uncooperative space objects: A case of multi-platform fusion, *Adv. Sp. Res.*
522 62 (2018) 2665–2678. doi:10.1016/j.asr.2018.07.031.

- 523 [21] C. Bonnal, J.M. Ruault, M.C. Desjean, Active debris removal: Recent progress and current trends, *Acta Astronaut.* 85 (2013) 51–60.
524 doi:10.1016/j.actaastro.2012.11.009.
- 525 [22] Y. Guo, F. Sohel, M. Bennamoun, M. Lu, J. Wan, Rotational Projection Statistics for 3D Local Surface Description and Object
526 Recognition, *Int. J. Comput. Vis.* 105 (2013) 63–86. doi:10.1007/s11263-013-0627-y.
- 527 [23] R.P. Kornfeld, R.L. Bunker, G.C. Cucullu, J.C. Essmiller, F.Y. Hadaegh, C. Christian Liebe, C.W. Padgett, E.C. Wong, New
528 millennium ST6 autonomous rendezvous experiment (ARX), in: 2003 IEEE Aerosp. Conf. Proc. (Cat. No.03TH8652), IEEE, 2003: pp.
529 1–380. doi:10.1109/AERO.2003.1235067.
- 530 [24] M. Estébanez Camarena, L.M. Feetham, A. Scannapieco, N. Aouf, FPGA-based multi-sensor relative navigation in space: Preliminary
531 analysis in the framework of the I3DS H2020 project, in: 69 Th Int. Astronaut. Congr. (IAC), International Astronautical Federation,
532 Bremen, 2018: pp. 1–8.
- 533 [25] P.J. Besl, N.D. McKay, A method for registration of 3-D shapes, *IEEE Trans. Pattern Anal. Mach. Intell.* 14 (1992) 239–256.
534 doi:10.1109/34.121791.
- 535 [26] R. Opromolla, G. Fasano, G. Rufino, M. Grassi, Uncooperative pose estimation with a LIDAR-based system, *Acta Astronaut.* 110
536 (2015) 287–297. doi:10.1016/j.actaastro.2014.11.003.
- 537 [27] L. Liu, G. Zhao, Y. Bo, Point cloud based relative pose estimation of a satellite in close range, *Sensors (Switzerland)*. 16 (2016).
538 doi:10.3390/s16060824.
- 539 [28] A. Rhodes, E. Kim, J.A. Christian, T. Evans, LIDAR-based Relative Navigation of Non-Cooperative Objects Using Point Cloud
540 Descriptors, in: AIAA/AAS Astrodyn. Spec. Conf., American Institute of Aeronautics and Astronautics, Reston, Virginia, 2016.
541 doi:10.2514/6.2016-5517.
- 542 [29] A. Aldoma, F. Tombari, R.B. Rusu, M. Vincze, OUR-CVFH – Oriented, Unique and Repeatable Clustered Viewpoint Feature
543 Histogram for Object Recognition and 6DOF Pose Estimation, in: *Lect. Notes Comput. Sci. (Including Subser. Lect. Notes Artif. Intell.*
544 *Lect. Notes Bioinformatics)*, 2012: pp. 113–122. doi:10.1007/978-3-642-32717-9_12.
- 545 [30] A.E. Johnson, M. Hebert, Using spin images for efficient object recognition in cluttered 3D scenes, *IEEE Trans. Pattern Anal. Mach.*
546 *Intell.* 21 (1999) 433–449. doi:10.1109/34.765655.
- 547 [31] A.P. Rhodes, J.A. Christian, T. Evans, A Concise Guide to Feature Histograms with Applications to LIDAR-Based Spacecraft Relative
548 Navigation, *J. Astronaut. Sci.* 64 (2017) 414–445. doi:10.1007/s40295-016-0108-y.
- 549 [32] A.B. Dietrich, J.W. McMahon, Robust Orbit Determination with Flash Lidar Around Small Bodies, *J. Guid. Control. Dyn.* 41 (2018)
550 2163–2184. doi:10.2514/1.G003023.
- 551 [33] A. Dietrich, J.W. McMahon, Orbit Determination Using Flash Lidar Around Small Bodies, *J. Guid. Control. Dyn.* 40 (2017) 650–665.
552 doi:10.2514/1.G000615.
- 553 [34] O. Kechagias-Stamatis, N. Aouf, D. Nam, 3D Automatic Target Recognition for UAV Platforms, in: 2017 Sens. Signal Process. Def.
554 Conf., IEEE, London, UK, 2017: pp. 1–5. doi:10.1109/SSPD.2017.8233223.
- 555 [35] O. Kechagias-Stamatis, N. Aouf, M.A. Richardson, 3D automatic target recognition for future LIDAR missiles, *IEEE Trans. Aerosp.*
556 *Electron. Syst.* 52 (2016) 2662–2675. doi:10.1109/TAES.2016.150300.
- 557 [36] H. Bay, A. Ess, T. Tuytelaars, L. Van Gool, Speeded-Up Robust Features (SURF), *Comput. Vis. Image Underst.* 110 (2008) 346–359.

558 doi:10.1016/j.cviu.2007.09.014.

559 [37] Jianbo Shi, Tomasi, Good features to track, in: Proc. IEEE Conf. Comput. Vis. Pattern Recognit. CVPR-94, IEEE Comput. Soc. Press,
560 1994: pp. 593–600. doi:10.1109/CVPR.1994.323794.

561 [38] D.G. Lowe, Distinctive image features from scale invariant keypoints, *Int. J. Comput. Vis.* 60 (2004) 91–110.
562 doi:10.1023/B:VISI.0000029664.99615.94.

563 [39] P. Viola, M. Jones, Robust real-time face detection, *Int. J. Comput. Vis.* 57 (2004) 137–154.

564 [40] C. Harris, M. Stephens, A Combined Corner and Edge Detector, in: *Proceedings Alvey Vis. Conf. 1988*, Alvey Vision Club, 1988: p.
565 23.1-23.6. doi:10.5244/C.2.23.

566 [41] P.F. Alcantarilla, A. Bartoli, A.J. Davison, KAZE features, in: *Lect. Notes Comput. Sci. (Including Subser. Lect. Notes Artif. Intell.*
567 *Lect. Notes Bioinformatics)*, 2012: pp. 214–227. doi:10.1007/978-3-642-33783-3_16.

568 [42] A. Alahi, R. Ortiz, P. Vandergheynst, FREAK: Fast Retina Keypoint, in: *2012 IEEE Conf. Comput. Vis. Pattern Recognit., IEEE*,
569 2012: pp. 510–517. doi:10.1109/CVPR.2012.6247715.

570 [43] S. Leutenegger, M. Chli, R.Y. Siegwart, BRISK: Binary Robust invariant scalable keypoints, *2011 Int. Conf. Comput. Vis.* (2011)
571 2548–2555. doi:10.1109/ICCV.2011.6126542.

572 [44] O. Kechagias-Stamatis, N. Aouf, G. Gray, L. Chermak, M. Richardson, F. Oudyi, Local feature based automatic target recognition for
573 future 3D active homing seeker missiles, *Aerosp. Sci. Technol.* 73 (2018) 309–317. doi:10.1016/j.ast.2017.12.011.

574 [45] M. Muja, D.G. Lowe, Fast Approximate Nearest Neighbors with Automatic Algorithm Configuration, in: *Int. Conf. Comput. Vis.*
575 *Theory Appl. (VISAPP '09)*, Lisboa, Portugal, 2009: pp. 1–10. doi:10.1.1.160.1721.

576 [46] H. Chen, B. Bhanu, 3D free-form object recognition in range images using local surface patches, *Pattern Recognit. Lett.* 28 (2007)
577 1252–1262. doi:10.1016/j.patrec.2007.02.009.

578 [47] A. Amamra, N. Aouf, D. Stuart, M. Richardson, A recursive robust filtering approach for 3D registration, *Signal, Image Video Process.*
579 10 (2016) 835–842. doi:10.1007/s11760-015-0823-z.

580 [48] D. Simon, Kalman Filtering, *Embed. Syst. Program.* (2001) 72–79.

581 [49] Y. Guo, M. Bennamoun, F. Sohel, M. Lu, J. Wan, N.M. Kwok, A Comprehensive Performance Evaluation of 3D Local Feature
582 Descriptors, *Int. J. Comput. Vis.* 116 (2016) 66–89. doi:10.1007/s11263-015-0824-y.

583 [50] O. Kechagias-Stamatis, N. Aouf, Histogram of distances for local surface description, in: *2016 IEEE Int. Conf. Robot. Autom., IEEE*,
584 *Stockholm, Sweden*, 2016: pp. 2487–2493. doi:10.1109/ICRA.2016.7487402.

585 [51] J. Krizaj, V. Struc, F. Mihelic, A feasibility study on the use of binary keypoint descriptors for 3D face recognition, in: *Mex. Conf.*
586 *Pattern Recognit.*, 2014: pp. 142–151. doi:10.1007/978-3-319-07491-7_15.

587 [52] J. Heinly, E. Dunn, J. Frahm, Comparative Evaluation of Binary Features, in: *Comput. Vis. -- ECCV 2012*, Springer Berlin Heidelberg,
588 2012: pp. 759–773. doi:10.1007/978-3-642-33709-3_54.

589 [53] O. Kechagias-Stamatis, N. Aouf, Fast 3D object matching with Projection Density Energy, in: *2015 23rd Mediterr. Conf. Control*
590 *Autom. MED 2015 - Conf. Proc., IEEE*, 2015: pp. 752–758. doi:10.1109/MED.2015.7158836.

591